Grain-Boundary-Enhanced Carrier Collection in CdTe Solar Cells

Chen Li,[1,2] Yelong Wu,[3] Jonathan Poplawsky,[4,2] Timothy J. Pennycook,[5,6] Naba Paudel,[3] Wanjian Yin,[3] Sarah J. Haigh,[7] Mark P. Oxley,[8,2] Andrew R. Lupini,[2] Mowafak Al-Jassim,[9] Stephen J. Pennycook,[4] and Yanfa Yan[3]

[1]*Department of Chemistry, Vanderbilt University, Nashville, Tennessee 37235, USA*
[2]*Materials Science and Technology Division, Oak Ridge National Laboratory, Oak Ridge, Tennessee 37831, USA*
[3]*Department of Physics and Astronomy, The University of Toledo, Toledo, Ohio 43606, USA*
[4]*Department of Materials Science and Engineering, University of Tennessee, Knoxville, Tennessee 37996, USA*
[5]*Department of Materials, University of Oxford, Oxford OX13PH, United Kingdom*
[6]*SuperSTEM Laboratory, Daresbury WA44AD, United Kingdom*
[7]*School of Materials, University of Manchester, Manchester M139PL, United Kingdom*
[8]*Department of Physics and Astronomy, Vanderbilt University, Nashville, Tennessee 37235, USA*
[9]*The Measurements and Characterization Group, National Renewable Energy Laboratory, Golden, Colorado 80401, USA*

(Received 18 December 2013; published 16 April 2014)

When CdTe solar cells are doped with Cl, the grain boundaries no longer act as recombination centers but actively contribute to carrier collection efficiency. The physical origin of this remarkable effect has been determined through a combination of aberration-corrected scanning transmission electron microscopy, electron energy loss spectroscopy, and first-principles theory. Cl substitutes for a large proportion of the Te atoms within a few unit cells of the grain boundaries. Density functional calculations reveal the mechanism, and further indicate the grain boundaries are inverted to *n* type, establishing local *p*-*n* junctions which assist electron-hole pair separation. The mechanism is electrostatic, and hence independent of the geometry of the boundary, thereby explaining the universally high collection efficiency of Cl-doped CdTe solar cells.

DOI: 10.1103/PhysRevLett.112.156103 PACS numbers: 68.37.Ma, 61.72.Mm, 73.50.Gr, 88.40.jm

Cadmium telluride (CdTe) was first established as a viable low-cost photovoltaic material over 26 years ago [1–4], through a passivation process involving $CdCl_2$. The large efficiency enhancements resulting from the treatment have remained crucial ever since, even as cell efficiencies have steadily risen to reach the current record of 19.6% [5]. However, despite decades of speculation [6–14], the success of the $CdCl_2$ treatment has remained a mystery: many different mechanisms have been proposed. It has been suggested that $CdCl_2$ heat treatment might promote grain growth and recrystallization [6,7], enhance S diffusion or S-Te interdiffusion [8,9], passivate deep defect levels within the band gap [6,10,11], or optimize carrier collection [12–14].

One important fact is that after $CdCl_2$ heat treatment, polycrystalline CdTe cells are far superior to cells based on single crystals [15], which is particularly surprising as grain boundaries (GBs) typically act as nonradiative recombination centers [16,17]. This indicates that the interaction between the $CdCl_2$ treatment and grain boundaries is the key to high efficiency solar cells. In order to figure out this interaction, we have grown CdTe cells without and with $CdCl_2$ treatment, and performed electron beam induced current (EBIC) imaging on them, as shown in Fig. 1. Without $CdCl_2$ treatment the boundaries appear dark, indicating strong carrier recombination; however, after the $CdCl_2$ treatment they become highly efficient current collectors, much more efficient than the grain interiors [18,19]. So it is clear that the $CdCl_2$ treatment dramatically improves the efficiency of the GBs. To understand how this occurs, a direct correlation of the atomic and electronic structure of GBs is critical.

In this Letter we determine the electrical activity, atomic scale composition, and electronic structure of the boundaries through the combination of state-of-the-art electron microscopy and density functional theory (DFT) simulations. Our findings demonstrate that grain boundaries, which would normally act as recombination centers, after treatment, actually separate the photogenerated electron hole pairs through local electric fields, thereby actively contributing to cell performance. Cl atoms substitute for Te atoms within a few unit cells of the GBs in sufficiently high concentrations to invert the boundary regions from *p* to *n* type. As the grains remain *p* type, the inversion of the GBs results in local electric fields that maintain separate segregated conduction pathways for electrons and holes. The mechanism is electrostatic, and hence independent of the geometry of the boundary, which explains the universal benefit of the $CdCl_2$ treatment. This microscopic understanding of the role of Cl points to new directions to further improve cell efficiency.

CdTe solar cells were deposited on CdS window layers via close-space sublimation, followed by the $CdCl_2$ heat treatment. EBIC imaging was performed with a Hitachi S4800-FEG scanning electron microscope. Atomic resolution scanning transmission electron microscopy (STEM) images and electron energy loss spectroscopy (EELS) spectra were acquired with a Nion UltraSTEM 200 microscope

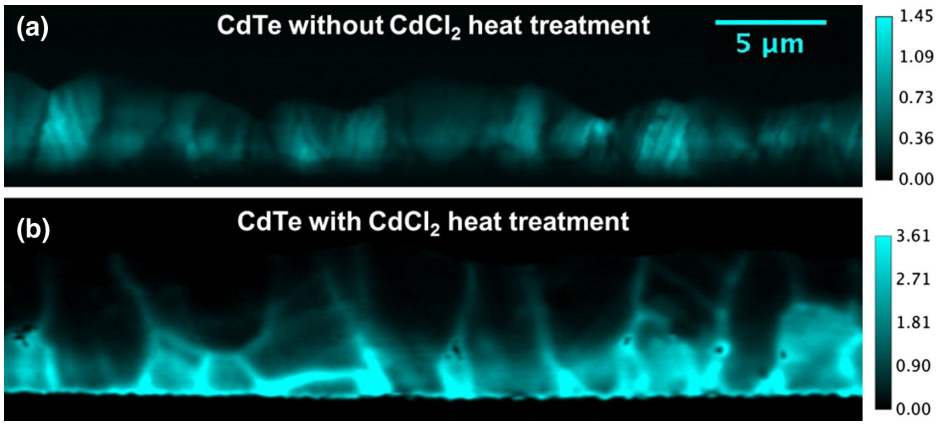

FIG. 1 (color online). Cross section EBIC maps of (a) a CdTe solar cell without $CdCl_2$ treatment showing dark contrast on the GBs, (b) a $CdCl_2$ treated cell showing high current collection at the GBs.

[20,21] equipped with a Gatan Enfinium EEL spectrometer. Cl L_{23}, Cd M_{45}, and Te M_{45} edges were used for the EELS profiles and elemental maps. Energy dispersive x-ray maps were obtained at 200 kV in an FEI Titan ChemiSTEM. Hubbard U correction has been used in the DFT calculations [22,23], giving a calculated band gap of 0.9 eV for bulk CdTe. More experimental and calculational details are in the Supplemental Material [24].

We employ state-of-art aberration-corrected scanning transmission electron microscopy and electron energy-loss spectroscopy to determine the structure and composition of the GBs with subangstrom resolution. As STEM Z-contrast images are sensitive to atomic number, we are able to distinguish Cd and Te columns directly from their image intensities. Since column intensity at the GB cores can be affected by strain, impurities, or vacancies, we identify the Cd-Te polarity at the cores by extrapolating from the surrounding perfect crystal [25–27]. The STEM Z-contrast image in Fig. 2(a) shows the atomic structure of a typical Σ9 coincidence site lattice (CSL) [28] GB in $CdCl_2$-treated CdTe. Viewed along the [110] zone axis, the measured misorientation angle between the grains at the two sides of this GB is close to 141°, which indicates it is a CSL Σ9 GB. The yellow solid boxes indicate symmetric (114) Σ9 GBs, while the green dashed box marks a short asymmetric (111)/(001)Σ9 GB. The asymmetric Σ9 GB segment is only about 1 nm long, indicating the symmetric Σ9 GB is more energetically favorable. The Cd and Te columns at the GB are marked by small blue and large yellow circles, respectively. Periodic Cd_3Te core configurations, which are indicated with white dashed circles, are observed along the entire GB at both symmetric and asymmetric regions. As there are three single Cd columns and one single Te column in each dislocation core structure, we call this GB a Cd-core Σ9 GB. To further investigate the 3D configuration of this GB, a through focal series movie with ten frames was acquired (see movie 1 in the Supplemental Material [24]), which shows the angle of the GB is inclined about 4.0° to the [110] zone axis, so it is likely that there are kinks along the dislocation cores about 5 nm apart. This is comparable to our depth of focus, explaining why we see clear atomic resolution images.

The Cd_3Te core configurations are also observed at complex partial dislocations, which are the junction of two stacking faults. Figure S1(a1) in the Supplemental Material [24] shows two adjacent Cd_3Te cores where two extrinsic stacking faults join together. The misorientation angle between the two extrinsic stacking faults is very close to the misorientation angle of the Σ9 GB, which explains why this complex partial dislocation has a similar core configuration. We have also observed a $CdTe_3$ core [Fig. S1(b1) in

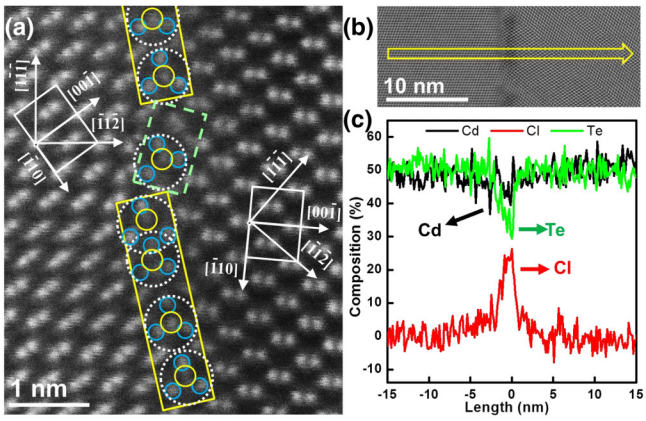

FIG. 2 (color online). Atomic structure and elemental distribution of the GB. (a) STEM Z-contrast image showing a Σ9 GB with symmetric (yellow boxes) and asymmetric (green dashed box) segments. The basic components of both the symmetric and asymmetric Σ9 GBs are Cd_3Te dislocation cores (white dashed circles). The small blue and large yellow solid circles indicate single Cd and Te columns, respectively. (b) An EELS line scan was taken along the yellow arrow, and (c) the resulting composition profiles show strong Cl enrichment and Te reduction confined to a $1 \sim 2$ nm range at the GB.

the Supplemental Material [24]], with a similar configuration but the opposite polarity. Based on the similarity of the Cd_3Te complex partial dislocation core and the Cd-core Σ9 GB, we anticipate that the opposite polarity $CdTe_3$ core configuration is also a possible grain boundary structural unit, which would form a Te-core Σ9 GB. Both of these Cd-core and Te-core complex partial dislocations have also been found in untreated CdTe, with no obvious difference in structure.

To detect any Cl segregation and associated compositional changes, spectrum imaging was performed on both Cd-core and Te-core complex partial dislocations, as shown in Fig. S1(a2, a3, b2, b3). Clear Cl enrichment was detected at both types of dislocations. Similar Cl segregation is found at the Cd-core Σ9 GB, as shown in Figs. 2(b) and 2(c). Remarkably, from the grain to the GB, the measured Cl concentration rises to about 25%, while the Te concentration decreases by a similar amount. The Cd concentration is almost constant, indicating that about 50% of the Te sites are filled by Cl. The measured concentration in a GB core can be affected by electron channeling effects; however, it is clear that very significant amounts of Cl atoms have doped into Te sites (Cl_{Te} dopants) in a very confined area at the GB. Both Cl and Te EELS profiles show Gaussian distributions with ~1 nm full width at half maximum (FWHM). The true Cl doping should be even narrower with higher concentration both because of the 4.0° tilt to the beam direction and because of beam broadening/channeling effects, as we discuss later. A similar apparent Cl enrichment and Te decrease is observed in a cell treated by both $CdCl_2$ and Cu treatments, see Fig. S2 in the Supplemental Material [24]. Moreover, not only these CSL GBs, but also all the random GBs examined show major substitution of Cl for Te (Fig. S3 of the Supplemental Material [24]). The essential result would therefore appear to be quite general, and is not observed in untreated GBs, see Fig. S4 in the Supplemental Material [24].

Based on the atomic resolution STEM images, a model of the Cd-core Σ9 GB was constructed [Fig. 3(a)]. DFT was used to relax the structure and determine the Cl segregation energy profile across the GB [Fig. 3(b)]. The profile shows Cl substitution to be energetically favored in a very narrow region in and around the GB, with the segregation energy dropping from its maximum 0.5 eV to zero only 0.8 nm from the center of the GB, implying a segregation width of 1–2 nm. This is in good agreement with the EELS profile.

To understand the effect of Cl segregation, the electronic properties of the Cd-core Σ9 GB with and without Cl segregation have been calculated using DFT. It was found that at the GB plane, the Cd atoms have a weak interaction along the viewing X direction, forming Cd-Cd dimers at the GB plane. For the same reason, Te-Te dimers have also formed. Such Cd-Cd and Te-Te interactions lead to the formation of GB states indicated by the arrows in the calculated band structure [Fig. 3(c)]. The Cd-Cd s-orbital

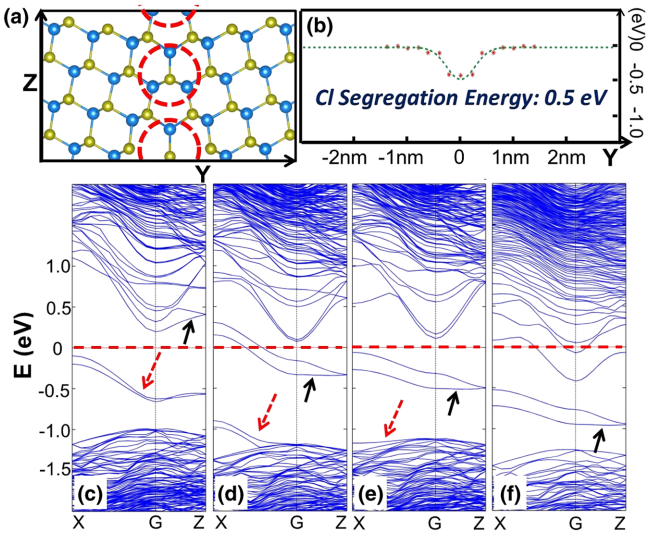

FIG. 3 (color online). (a) The center part of the Cd-core Σ9 GB supercell for DFT calculation, which contains two Cd_3Te dislocation cores (red dashed circles). (b) The calculated Cl segregation energy profile. The calculated band structures for the supercell containing (c) zero, (d) two, (e) four, and (f) five Cl atoms doped in Te sites. Cd-Cd bonding states and Te(Cl)-Te(Cl) antibonding states are indicated by red dashed and black solid arrows, respectively. The red dashed lines at zero energy in (c)–(f) indicate the positions of the highest occupied states. In (f) the boundary has turned n type.

interactions should lead to two low-energy occupied bonding states and two high-energy empty antibonding states. Detailed analysis using site-projected density of states revealed that the two occupied bonding states are inside the band gap as indicated by the red dashed arrow in Fig. 3(c). The two empty antibonding states are much higher in energy than the conduction band minimum (CBM) and are not shown in Fig. 3(c). The Te-Te p-orbital interactions also produce both occupied bonding and unoccupied antibonding states, which are much lower in energy than the respective Cd-Cd bonding and antibonding states. The occupied Te-Te bonding states are located deep inside the valence band, while the two unoccupied Te-Te antibonding states are located near the CBM and are indicated by the black solid arrow in Fig. 3(c). The red dashed lines in Figs. 3(c)–3(f) indicate the energy positions of the highest occupied states, which are set to zero.

When Cl atoms segregate into Te sites at the GB they cause important changes to the GB states and electrical properties of the GB. For instance when one Cl atom per core segregates into the GB the Te-Te interaction becomes a lower energy Te-Cl interaction instead, dropping the antibonding states deeper into the band gap. The extra electrons from the dopant atoms half fill the Te-Cl antibonding states, leaving the Cl atoms positively charged and introducing an electrostatic potential. This potential reduces the energy of the occupied Cd-Cd bonding states, pushing them down

to near the valence band maximum (VBM) [Fig. 3(d)]. When the number of Cl atoms incorporated into the GB is increased to two per core, the new Cl-Cl antibonding states become even lower in energy. The charge transfer increases the number of positively charged Cl atoms strengthening the electrostatic potential and pushing the occupied Cd-Cd bonding states right down into the valence band [Fig. 3(e)]. Further incorporation of Cl atoms should donate electrons to the conduction band and therefore make the system *n* type. Indeed, adding just one more substitutional Cl atom in the supercell puts the highest occupied state clearly in the conduction band, Fig. 3(f). Therefore, four Cl atoms per unit cell is the threshold for making the system *n* type. Such strong segregation is in fact energetically favorable, the segregation energy increasing from 0.5 eV/atom for two Cl atoms to 0.9 eV/atom for five Cl atoms.

We next estimate whether the GB plane observed with EELS contains sufficient Cl to create a type inversion by comparing the data to Cl, Te, and Cd profiles simulated for the GB model shown in Fig. S5 in the Supplemental Material [24]. The FWHM of the simulated Cl profile is ~ 0.8 nm, again in good agreement with the data. Although the model contains 25% Cl occupation (i.e., 50% Cl on Te sites) on the central three GB planes, the simulation shows that we would measure only about 18%. The discrepancy is because much of the electron beam is scattered (broadened) as it propagates through the thickness of the crystal, so that the apparent concentration is less than that actually present. This shows that the experimental measurement of 25% Cl substitution in the Cd-core Σ9 GB significantly underestimates the actual concentration, which therefore exceeds that necessary to make the GB region *n* type. Moreover, a weak segregation energy exists two and three planes away from the GB center, where there is no dislocation core, just elastic strain. Weak Cl segregation would be expected here also, bringing extra electrons to extend the *n*-type region.

It is important to note that we can generalize these results from the Σ9 GB to the random boundaries to explain their similar electronic behavior in EBIC imaging. From the Σ9 GB we know the mechanism is electrostatic in nature, resulting from the wrong Te-Te and Cd-Cd bonds and the electrons donated by the Cl atoms. In Fig. S6 of the Supplemental Material [24] we present similar conclusions concerning Te-core GBs, where segregation of Cl again leads to an *n*-type boundary. The exact geometry is unimportant to first order; the type inversion just depends on the number of wrong bonds and Cl atoms per unit area of the grain boundary plane. Boundaries of other angles will have a different density of structural units in the boundary plane, but will generate structures that contain the same basic Cd-Cd and Te-Te wrong bonds, as these are the only basic structural units that can exist apart from point defects. Therefore, these conclusions can be expected to hold for boundaries of arbitrary angle, the so-called random grain boundaries. The exact Cl concentration may vary by a factor of 2 or so, depending on the overall concentration of the wrong bonds, but these results strongly imply that any grain boundary will absorb sufficient Cl to clean the gap and turn the material *n* type, explaining the EBIC observations. Note that twin boundaries are not counted as normal GBs here, as they do not have the Te-Te and Cd-Cd wrong bonds [25]. Not surprisingly, neither Cl segregation nor enhanced EBIC signals have been observed at twin boundaries.

We conclude that all GBs will have sufficiently strong, localized, Cl segregation to cause the formation of a *p*-*n*-*p* junction across the GB, as shown in the sketch in Fig. 4. The built-in field formed in the regions between the GB and grain interior (GI) will help separate photogenerated carriers, and therefore reduce the carrier recombination rate. Electrons are attracted by the GBs while holes are repelled, which make the GBs and GIs segregated conduction pathways for electrons and holes. The enhanced carrier separation will also reduce the cathodoluminescence intensity from the GB regions, in agreement with observations [29]. The existence of depleted GBs and inverted GB models, based on scanning capacitance microscopy [14], scanning Kelvin probe force microscopy [30], scanning spreading resistance microscopy [30], EBIC imaging [31], and optical beam-induced currents [32] have been proposed before. Our result demonstrates the origin of the band bending is the substitution of a large fraction of the Te sites at the GB plane by Cl. In general, whether the Cl concentration at the GBs is sufficient for type inversion is likely to depend on the exact synthesis and post-treatment processes used [33].

To summarize, using EBIC imaging, we revealed a significant collection current enhancement at the GBs of CdTe after $CdCl_2$ treatment alone. The atomic structure of a Cd-core Σ9 GB has been determined using aberration-corrected STEM. Simultaneous EELS shows that Cl has substituted for about 50% of the Te sites within a narrow range (1–2 nm) at the GBs. The Cl segregation energy profile across the GB calculated with DFT matches the narrow Cl EELS profile. We have shown that the observed Cl concentration is sufficient to invert the GBs to *n* type, therefore creating *p*-*n* junctions between the grain interiors and the GBs. This GB inversion maintains carrier separation, separates the conduction pathways for electrons and holes, and provides a long awaited explanation of the universal nature of the efficiency enhancements $CdCl_2$

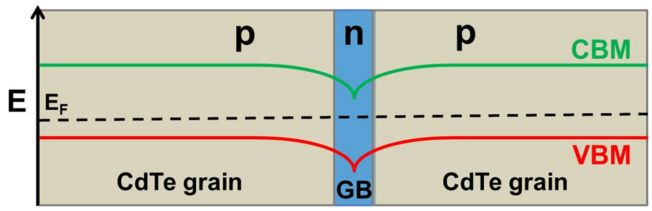

FIG. 4 (color online). A sketch showing the band diagram of the *p*-*n*-*p* junction at the GB.

treatment brings to polycrystalline CdTe-based solar cells. It further implies that grain boundary engineering, for example a higher density of columnar grains allowing free flow of holes and electrons to the back and front contacts, may improve cell efficiency even further.

This research was supported by the U.S. Department of Energy (DOE) Office of Energy Efficiency and Renewable Energy, Foundational Program to Advance Cell Efficiency (F-PACE) (C. L., J. P., Y. L. W., N. P., M. A. J., Y. Y., S. J. P.), and Office of Basic Energy Sciences (BES), Materials Science and Engineering Division (A. R. L.), DOE Grant No. DE-FG02-09R46554 (M. P. O.). Research was sponsored in part by the UK Engineering and Physical Sciences Research Council through the UK National Facility for Aberration-Corrected STEM (SuperSTEM), (T. J. P, S. J. H.) and through a user project supported by ORNL's Center for Nanophase Materials Sciences (CNMS), which is also sponsored by DOE-BES. This research used resources of the National Energy Research Scientific Computing Center, which is supported by the DOE Office of Science under Contract No. DE-AC02-05CH11231. Y. Y. acknowledges the support of the Ohio Research Scholar Program (ORSP).

[1] P. V. Meyers, C. H. Liu, and T. J. Frey, U.S. Patent No. 4,710,589 (1987).
[2] R. E. Treharne, B. L. Williams, L. Bowen, B. G. Mendis, and K. Durose, in *Photovoltaic Specialists Conference (PVSC), 38th IEEE, Austin, TX, 2012* (IEEE, Singapore, 2012) doi:10.1109/PVSC.2012.6317985 pp. 001983–001987.
[3] R. W. Birkmire and E. Eser, Annu. Rev. Mater. Sci. **27**, 625 (1997).
[4] R. W. Birkmire and B. E. McCandless, Curr. Opin. Solid State Mater. Sci. **14**, 139 (2010).
[5] M. A. Green, K. Emery, Y. Hishikawa, W. Warta, and E. D. Dunlop, Prog. Photovoltaics **21**, 1 (2013).
[6] H. R. Moutinho, M. M. Al-Jassim, D. H. Levi, P. C. Dippo, and L. L. Kazmerski, J. Vac. Sci. Technol. A **16**, 1251 (1998).
[7] B. E. McCandless, L. V. Moulton, and R. W. Birkmire, Prog. Photovoltaics **5**, 249 (1997).
[8] W. K. Metzger, D. Albin, M. J. Romero, P. Dippo, and M. Young, J. Appl. Phys. **99**, 103703 (2006).
[9] M. Terheggen, H. Heinrich, G. Kostorz, A. Romeo, D. Baetzner, A. N. Tiwari, A. Bosio, and N. Romeo, Thin Solid Films **431–432**, 262 (2003).
[10] V. Komin, B. Tetali, V. Viswanathan, S. Yu, D. L. Morel, and C. S. Ferekides, Thin Solid Films **431–432**, 143 (2003).
[11] L. Zhang, J. L. F. Da Silva, J. Li, Y. Yan, T. A. Gessert, and S.-H. Wei, Phys. Rev. Lett. **101**, 155501 (2008).
[12] S. A. Ringel, A. W. Smith, M. H. MacDougal, and A. Rohatgi, J. Appl. Phys. **70**, 881 (1991).
[13] I. Visoly-Fisher, S. R. Cohen, K. Gartsman, A. Ruzin, and D. Cahen, Adv. Funct. Mater. **16**, 649 (2006).
[14] I. Visoly-Fisher, S. R. Cohen, A. Ruzin, and D. Cahen, Adv. Mater. **16**, 879 (2004).
[15] A. Bosio, N. Romeo, A. Podesta, S. Mazzamuto, and V. Canevari, Cryst. Res. Technol. **40**, 1048 (2005).
[16] G. Beaucarne, S. Bourdais, A. Slaoui, and J. Poortmans, Appl. Phys. A **79**, 469 (2004).
[17] A. McEvoy, T. Markvart, and L. Castaner, *Practical Handbook of Photovoltaics: Fundamentals and Applications* (Elsevier Science, New York, 2003).
[18] O. Zywitzki, T. Modes, H. Morgner, C. Metzner, B. Siepchen, B. Späth, C. Drost, V. Krishnakumar, and S. Frauenstein, J. Appl. Phys. **114**, 163518 (2013).
[19] J. D. Poplawsky, N. Paudel, C. Li, C. Parish, D. Leonard, Y. Yan, and S. J. Pennycook (to be published).
[20] O. L. Krivanek, G. J. Corbin, N. Dellby, B. F. Elston, R. J. Keyse, M. F. Murfitt, C. S. Own, Z. S. Szilagyi, and J. W. Woodruff, Ultramicroscopy **108**, 179 (2008).
[21] O. L. Krivanek, N. Dellby, and A. R. Lupini, Ultramicroscopy **78**, 1 (1999).
[22] A. I. Liechtenstein, V. I. Anisimov, and J. Zaanen, Phys. Rev. B **52**, R5467 (1995).
[23] V. I. Anisimov, J. Zaanen, and O. K. Andersen, Phys. Rev. B **44**, 943 (1991).
[24] See Supplemental Material at http://link.aps.org/supplemental/10.1103/PhysRevLett.112.156103 for further experimental results and calculational details.
[25] C. Li, J. Poplawsky, Y. Wu, A. R. Lupini, A. Mouti, D. N. Leonard, N. Paudel, K. Jones, W. Yin, M. Al-Jassim, Y. Yan, and S. J. Pennycook, Ultramicroscopy **134**, 113 (2013).
[26] C. Li, Y. Wu, T. J. Pennycook, A. R. Lupini, D. N. Leonard, W. Yin, N. Paudel, M. Al-Jassim, Y. Yan, and S. J. Pennycook, Phys. Rev. Lett. **111**, 096403 (2013).
[27] C. Li, T. J. Pennycook, D. N. Leonard, K. Jones, Z. Wang, M. Al-Jassim, N. Paudel, Y. Yan, and S. J. Pennycook, MRS Proceedings, Vol. **1526**, doi:10.1557/opl.2013.569 (2013).
[28] H. Grimmer, W. Bollmann, and D. H. Warrington, Acta Crystallogr. Sect. A **30**, 197 (1974).
[29] B. G. Mendis, L. Bowen, and Q. Z. Jiang, Appl. Phys. Lett. **97**, 092112 (2010).
[30] C. S. Jiang, H. R. Moutinho, R. G. Dhere, and M. M. Al-Jassim, Phot. IEEE J. **3**, 1383 (2013).
[31] H. P. Yoon, P. M. Haney, D. Ruzmetov, H. Xu, M. S. Leite, B. H. Hamadani, A. A. Talin, and N. B. Zhitenev, Solar Energy Mater. Sol. Cells **117**, 499 (2013).
[32] S. Smith, P. Zhang, T. Gessert, and A. Mascarenhas, Appl. Phys. Lett. **85**, 3854 (2004).
[33] L. Kranz, C. Gretener, J. Perrenoud, D. Jaeger, S. S. A. Gerstl, R. Schmitt, S. Buecheler, and A. N. Tiwari, Adv. Energy Mater., doi:10.1002/aenm.201301400 (2013).